RESEARCH ARTICLE | NOVEMBER 13 2024

Switchable-magnetization planar probe MFM sensor for imaging magnetic textures of complex metal oxide perovskite

Michael Verhage ; H. Tunç Çiftçi ; Michiel Reul ; Tamar Cromwijk ; Thijs J. N. van Stralen ; Bert Koopmans ; Oleg Kurnosikov ; Kees Flipse

J. Appl. Phys. 136, 184504 (2024)
https://doi.org/10.1063/5.0234117

Journal of Applied Physics ARTICLE pubs.aip.org/aip/jap

Switchable-magnetization planar probe MFM sensor for imaging magnetic textures of complex metal oxide perovskite

Cite as: J. Appl. Phys. **136**, 184504 (2024); doi: 10.1063/5.0234117
Submitted: 20 August 2024 · Accepted: 23 October 2024 ·
Published Online: 13 November 2024

Michael Verhage,[1] H. Tunç Çiftçi,[2,3] Michiel Reul,[1,4] Tamar Cromwijk,[3,5] Thijs J. N. van Stralen,[1] Bert Koopmans,[3] Oleg Kurnosikov,[6] and Kees Flipse[1,a)]

AFFILIATIONS

[1]Eindhoven University of Technology—M2N, PO Box 513, 5600 MB Eindhoven, The Netherlands
[2]ARCNL, Contact Dynamics, Amsterdam, The Netherlands
[3]Eindhoven University of Technology—FNA, PO Box 513, 5600 MB Eindhoven, The Netherlands
[4]Lehrstuhl für Experimentalphysik (Festkörperphysik) und II. Physikalisches Institut, RWTH Aachen University, Aachen, Germany
[5]ARCNL, Computational Imaging, Amsterdam, The Netherlands
[6]University of Lorraine, Institut Jean Lamour, 54000 Nancy, France

[a)]**Author to whom correspondence should be addressed:** c.f.j.flipse@tue.nl

ABSTRACT

We introduce an alternative method for switching-magnetization magnetic force microscopy that utilizes planar tip-on-chip probes. Unlike conventional needle-like tips, the planar probe technique incorporates a microdevice near the tip apex on a 1×1 mm^2 chip, which allows for thin-film engineering and micro/nano-customization aimed at application-specific tip functionalization. In this study, we establish a microscale current pathway near the tip end to manage the tip magnetization state. This planar probe was used to investigate the intricate disordered magnetic domain structure of an epitaxial thin film of the transition metal oxide perovskite $LaMnO_3$, a material previously demonstrated to exhibit complex domains related to superparamagnetism, antiferromagnetism, and ferromagnetism. We successfully visualized an inhomogeneous distribution of magnetic islands near the Curie temperature, with a resolution exceeding 10 nm.

I. INTRODUCTION

Magnetic force microscopy (MFM) is a widespread method in fundamental surface studies and nanoscale technological applications with a high lateral resolution and pN force sensitivity.[1,2] The working principle of MFM relies on the force interaction between the tip's magnetic stray field and a samples' spatially varying magnetic textures. By nanoscale utilization of this magnetic force interaction, MFM covers a wide operational range from characterization to manipulation of magnetic objects.[3–5]

Despite its extensive use, a general MFM hits its capability limits mainly in lateral resolution of imaging materials with weak or time-varying magnetization. For instance, low coercive and weak ferromagnetic (FM) or superparamagnetic (SP) structures generally require an external magnetic field to saturate,[6] and without this the magnetic force to the tip is weak or may be undetectable. Furthermore, nonmagnetic interactions such as those of electrostatic origin can mask the magnetic signal.[7–9] To obtain the pure magnetic signal of nanoscale weak FM or SP textures, such as isolated islands, an MFM variant called switching magnetization force microscopy (SM-FM)[10,11] or controlled magnetization-MFM (CM-MFM)[8] stands out by extracting such signals out of the detected force.[9,11,12] Beyond traditional MFM, SM-FM measures a relative force change due to controlled altering of the magnetic state of the tip or the sample (or both). Only the magnetic field interaction is sensitive to the relative magnetic polarities between the tip and sample and hence can thus be detected. The need for a SM-FM imaging technique with the capability of imaging weak FM or SP islands with a resolution beyond 10 nm can be found in the study of

epitaxial complex oxide perovskites such as $LaMnO_3$ (LMO). Wang *et al.*[13] have shown that epitaxial LMO reveals an abrupt transition from an antiferromagnetic (AF) state to a FM state depending on the thickness of the LMO thin film. The magnetic transition occurred at a film of 5 atomic unit cell (u.c.) thickness. Furthermore, Anahory *et al.*[14] observed inhomogeneously distributed SP islands besides the FM domains, with the former only detected following an applied in-plane magnetic field of variable strength. Both groups used a scanning SQUID microscope (SSM), albeit with different lateral resolution, to image the LMO sample's stray field distribution. However, the SSM imaging performed by Anahory *et al.*[14] could not go beyond a resolution of 100 nm, which left the SP island size to be only indirectly inferred between 10 and 20 nm.

To solve the problem of limited imaging resolution of traditional MFM and for use in imaging complex oxide thin films, we designed a new type of SM-FM sensor. To this end, we design a magnetic tip with a stray field of several hundred mT strong enough to saturate the magnetic textures. The tip is realized by forming an oriented, single-domain magnetic state near the tip apex.[15] Traditional needle-like MFM tips generally only generate up to a few tens of mT of stray field.[2,16] With this approach, the LMO weak FM domains are simultaneously saturated and profiled for imaging by the same tip. The tip's stray field decays rapidly from the tip, and hence, by changing the height of the tip with respect to the sample surface the weak magnetic textures can be actively saturated.

We show that our sensor can image the magnetic textures of LMO with a resolution better than 10 nm. This advancement improves the traditional cantilever-based MFM techniques.[17,18] However, the imaging resolution also relies on the properties of the sample and the operational parameters of the MFM sensor, such as the amplitude of the oscillation and the spring constant of the cantilever.

We introduce an approach that combines planar chip-like probes[19–21] with highly sensitive tuning fork force sensors, which we refer to as the switching-magnetization planar probe (SM-PP). Figure 1(a) illustrates this sensor, highlighting specific channels for tip signaling and force measurement using the self-sensing tuning fork. The proposed method involves an on-chip reorientable tip magnetization that functions as a switchable magnetic force sensor without needing an external magnetic field. Moreover, the flat geometry of the planar probe tip facilitates the integration of future devices, aligning with that of MFM, and enables the use of additional scanning probe methods, such as SQUIDS-on-tip,[22] thermal detection and imaging,[23] as well as nitrogen-vacancy magnetometry.[24]

II. RESULTS AND DISCUSSION

A. Sensor design

The working principle of the SM-PP relies on switching from a multi-domain state of the tip to a poled single domain via an internally generated Ørsted field (H_p) within a planar chip-like probe, as illustrated in Figs. 1(a), 1(b), and 1(d). Initially, the magnetic layer on the tip is in a multi-domain state with a closed flux loop, Fig. 1(d). The direction of this flux may be irregular and hence inappropriate for controlled perturbing of weak FM or SP islands. The planar probe design used in this study has a bi-metallic structure of thin-film components: the current-carrying layer and the ferromagnetic layer, as depicted in Figs. 1(b) and 1(c). By sending an electrical pulse (I_p) through the current-carrying layer in a designated electrical pathway (called the bridge) near the tip apex, we generate an Ørsted field of controlled magnitude and well defined direction which magnetizes the ferromagnetic layer. This action leads to a singular domain state of the tip apex, with a preferable orientation depending on the pulse direction.

The planar probe is formed by cleaving a silicon wafer into a small 1 mm^2 square piece with a 90° tip apex.[19,25] Near the tip apex, i.e., the cleaved corner increases the flux density, increasing the tip stray field compared to a needle-like MFM tip. This magnetic field strength and distribution are discussed later on. The single domain state of the tip can be used to probe weak FM domains with SM-MFM. To this end, we used a 30 nm Pt film for the current-carrying layer and a 15 nm Co film for the ferromagnetic layer, placed on top of the planar probe. Detailed fabrication procedures of the film and planar probe are given in supplementary material S1.

Contrary to the traditional passive needle-like MFM tips, we can orient the SM-PP multi-domains into a singular domain by only a single current pulse as often as needed to combat transient tip demagnetization, a known issue in MFM. The resulting numerically calculated tip magnetization structure after sending a current pulse I_p is illustrated in Fig. 1(d). As a result, we can obtain consistently oriented tip domains, resulting in a predictable stray field in the vicinity of the tip, as indicated by $\vec{B}$ in Fig. 1(e). Figure 1(e) illustrates the side view of the SM-PP with the tip stray field distribution predominately out-of-plane from the sample's perspective. In supplementary material S4, Figs. S6–S8, and in the next section, we discuss in-depth the tip stray field distribution derived from a numerical study. Finally, Fig. 1(f) shows a Kerr microscopy image of the SM-PP, after having sent a current pulse I_p of sufficient magnitude. A single domain, poled tip is formed as observed with the dark contrast near the apex, highlighted within the dashed circle in the figure.

We attached this functionalized planar probe to a quartz tuning fork (QTF) force sensor[25] with integrated electrical access to the probe for the current pulse I_p, as schematically illustrated in Fig. 1(a). We used mass-retuning,[25] which entails the removal of mass of the QTF prong, that equates to the added mass of the probe. QTF's have been successfully used before for MFM[26] and are easily integrated in an ultrahigh vacuum (UHV) scanning probe microscope. The mass-retuning approach for tuning fork significantly improves the mass-carrying load capacity of the QTF.[25]

In the non-mass perturbed state of the QTF, the quality factor (Q-factor) can easily exceed 10^4–10^5. As widespread AFM and MFM applications using a QTF have previously experienced, once the probe mass already exceeds several tens of μg, which is far below the mass of a chip-like probe in this work, the QTF's Q-factor value drops to only several hundred.[27] This reduction in Q-factor results in a large loss in force sensing capabilities.[25,28] For degraded Q-factor sensors, we would be unable to use the planar probe to image the magnetic stray fields of the LMO. To this end, the mass-retuned tuning fork approach compensates for the mass unbalancing from planar probe attachment and recovers sensitivity. As a result, we are able to restore the Q-factor to greater than 2×10^4 at room temperature in UHV.[20,25] In supplementary material S3, we discuss further the need for a high Q further.

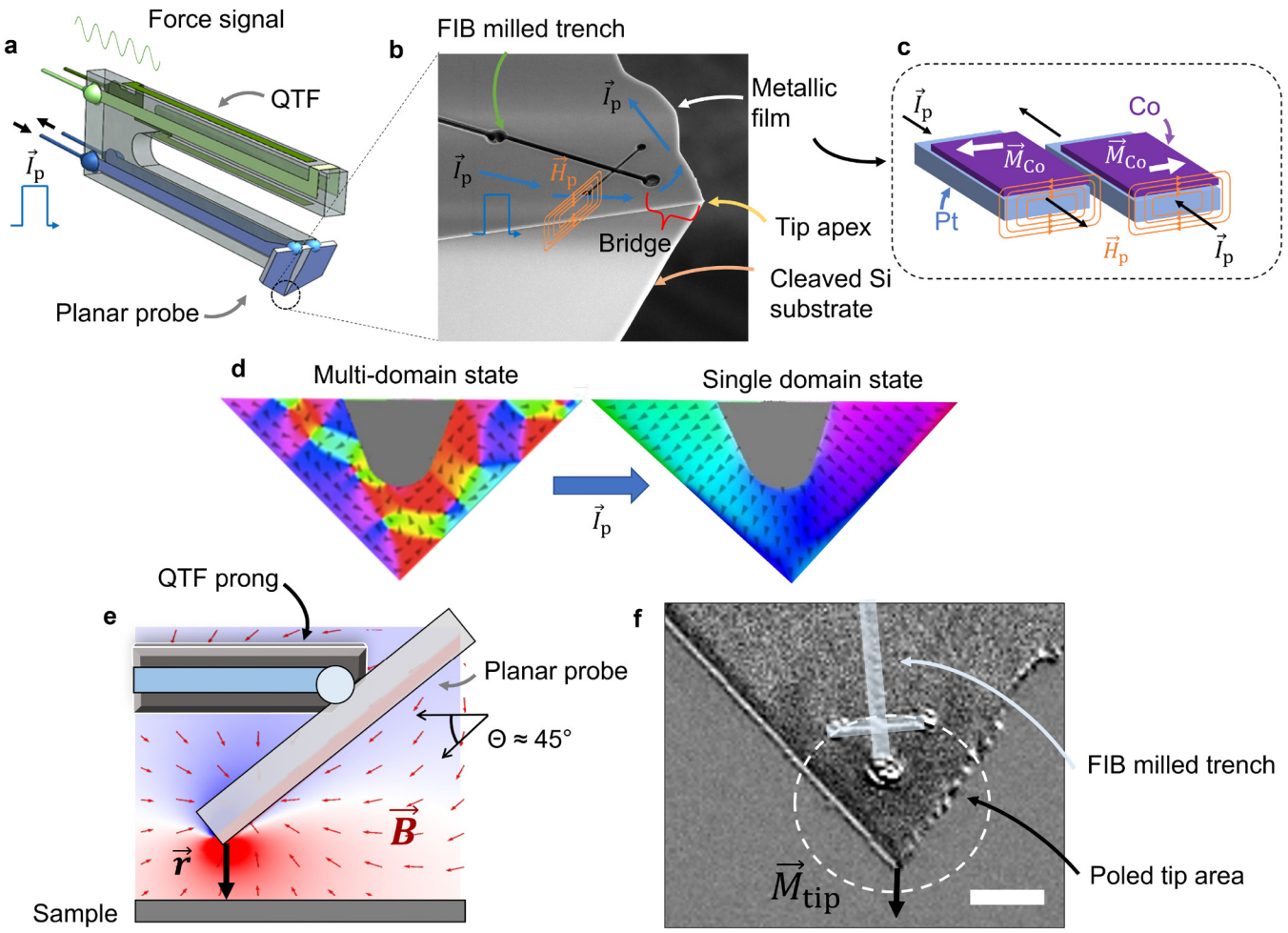

FIG. 1. Planar probe with switchable tip magnetization (SM-PP). (a) Illustration of the SM-PP sensor, with electrical contacts for force sensing and sending current pulses I_p to the tip apex. The tip is formed by a tip-on-chip called the planar probe (PP). (b) SEM image of the PP with a sharp tip apex formed by cleaving a Si wafer. Sending a current pulse generates an Ørsted field ($\vec{H}_p$) within the metallic film to orient the tip magnetization into a singular domain state. The current pathway is created by the formation of a FIB milled bridge. (c) The metallic film with two main layers: the current-carrying Pt layer and the ferromagnetic Co layer. The polarity of I_p determines the direction of the Ørsted field ($\vec{H}_p$) which alters (reverse) the direction of magnetization of the Co film. (d) Multi-domain state can be poled into an oriented single domain by a controlled current pulse. (e) Schematic side view of the SM-PP shows the mass retuned tuning fork prong and a lateral view of the surrounding tip stray field $\vec{B}$. The planar probe is placed under a 45° angle to the prong. (f) Kerr microscopy image showing a single domain magnetic tip state after sending a single I_p. The dark contrast at the bottom of the tip demonstrates the singular domain with magnetization $\vec{M}_{tip}$. The white scale bar equals 5 μm.

The degradation of the Q-factor can similarly occur due to extra wiring needed to connect the current control signal for pulse transmission to the planar probe tip apex for controlled magnetization. This is also true for combined AFM and STM qPlus, as well as the necessity to read-out the tunnel current, leading to the integration of dedicated electrical contacts on the tuning fork itself.[29] We restructure the electrodes as described in Ref. 25 by means of separation of the existing electrode layout. To conclude, we solve the mass imbalance introduced by the large mass of the planar probe by mass re-tuning[28] the QTF as described in our previous work[25] and using readily available electrodes on the tuning fork to prevent the need for additional external wiring for control of on-tip devices.

B. Numerical simulations of tip functioning

To extract the magnetic signal from weak ferromagnetic islands, the SM-PP must transition from a multi-domain state to a fully oriented single domain at the tip apex. We utilized finite element modeling (FEM) using COMSOL Multiphysics to simulate the Ørsted field generated within the bridge to determine the necessary I_p magnitude for controlling tip magnetization.

Additionally, we can investigate the thermal response of the tip by Joule heating.

Figure 2 presents the numerical and experimental validation of the magnetic switch of SM-PP tip. The simulations cover various bridge widths d in the range from 50 nm to 7 μm and different I_p values from 10 to 200 mA. The pulse duration is 500 ns. See supplementary material S4 for details on the simulations. First, Fig. 2(a) shows the calculated spatial field components of $\vec{H}_p(\vec{r})$ of

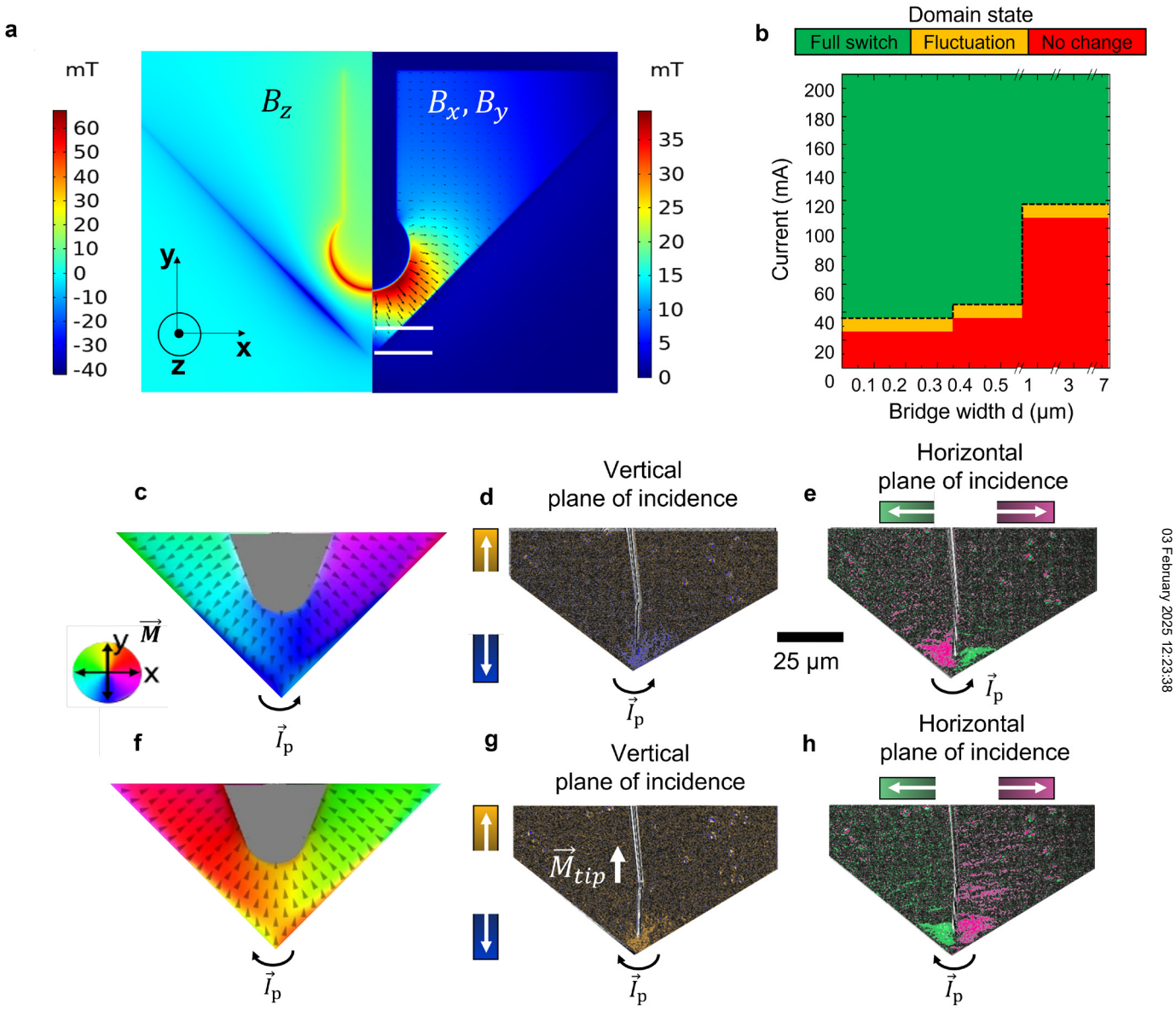

FIG. 2. Numerical and experimental validation of the magnetic switch of the SM-PP tip. (a) Numerical calculations of the generated Ørsted field $\vec{H}_p(\vec{r})$ magnetic field components B_z and B_x, B_y from a 150 mA current pulse I_p. The simulated bridge structure is 5 μm wide. The distance between the two white lines near the tip apex is equal to 1 μm and indicates low current density areas. For single domain nucleation and orientation, this area must also be controlled. (b) MuMax^3 calculation of the phase diagram of the switching of domains at the tip apex under increased current values I_p. The bridge width d, from the tip apex to the FIB milled trench, are varied from 50 nm to 7 μm, presented in the phase diagram. The colors indicate a switch between two oppositely poled single domain state (green), domain fluctuations (orange), or no switch (red). (c) and (f) Simulated single domain formation of the tip for reversing I_p polarity. (d)–(h) Kerr microscopy images show domain orientation switching after inverting I_p polarity. These images are taken from experiments. (d) and (g) The vertical component of the Co in-plane magnetization is observed to switch, indicated in blue and yellow false coloring, of the Kerr microscopy gray level signal, visible near the tip end (e) and (h) The horizontal component of the Co in-plane magnetization, false colored pink and green, is mainly located near the tip end.

a 5 μm bridge under application of I_p =150 mA. The in-plane field components B_x and B_y of $\vec{H}_p(\vec{r})$ follow the bridge structure. This indicates that both symmetric sides of the tip have opposing magnetic direction, as is evident from the current flow pathway. Near the tip apex, B_x and B_y are relatively small since the current density is lowest [between the white lines of Fig. 2(a)]. A strong out-of-plane component B_z [Fig. 2(a)] is only observed at the boundary of the tip and bridge, but is of little importance with respect to the in-plane magnetization of the Co film. At just 1 μm away from the tip apex, above the upper white line, the in-plane magnetic field is larger than 10 mT which implies the nucleation of oriented in-plane Co domains. In supplementary material S1 the magnetization response of the Co film is given.

Following, $\vec{H}_p(\vec{r})$ is used as an input parameter within Mumax[3] to calculate the magnetization response (switch vs no switch) of the Co film at the tip apex, as a function of the bridge width d and I_p. Details of the Mumax[3] calculations are given in supplementary material S4. In Fig. 2(b) the color scale represents three different states of the tip magnetization after applying I_p. Green means that the tip end domain shows a 180° reversal, so a full switch. Yellow represents an observed modification or a limited rotation by less than 180° in the tip domain. Red implies that the magnetization remained identical to the pre-pulse orientation. The results show a few tens of mA increase in critical current level for the bridge gap width values from 50 nm until 1 μm, as given in Fig. 2(a). For bridge gap widths greater than 1 μm, the critical current shows a larger increase, but saturates for increasingly larger widths. The simulations indicate that it is possible to fully nucleate a single-domain state following a sufficient current magnitude with a design freedom in bridge width sizes.

The magnetic field near the extremity is pivotal in saturating the weakly ferromagnetic domains of the sample under examination. We employed numerical simulations to illustrate the spatial distribution of the magnetic field B from the tip and its lateral propagation over the sample's surface, as depicted in supplementary material S4, Figs. S6–S8. The B_x and B_y components are most evident directly under the tip, showing localized magnetic fields reaching up to 350 mT. Achieving perfect symmetry in the tip's geometry within a constructed planar probe is challenging, and asymmetries can occur in both the bridge shape and its position at the tip's apex. Consequently, during experiments, one can anticipate higher in-plane field values beneath the tip. For LMO measurements, utilizing both in-plane and out-of-plane fields is advantageous: the in-plane field aids in magnetizing weak ferromagnetic or superparamagnetic regions, while the B_z component is used to measure the stray field force signal.

Although a nanometer scale of the bridge can potentially be achieved with various techniques and types of lithography, in our experiments, we used focused ion beam (FIB) milling. This resulted in bridges on the micrometer scale and, as the simulation results show of Fig. 2(b), we require a current magnitude in the order of 10^2 mA for domain inversion. Supplementary material S1 discusses the FIB fabrication in further detail. Using MuMax[3], we simulate a current pulse I_p with 130 mA amplitude and 500 ns duration for a bridge of 5 μm, the tip magnetization inverses completely according to the pulse polarity, as shown in Figs. 2(c) and 2(f). The notion of tip switch at values below 130 mA is important, especially for micrometer-scale bridges, because it significantly limits Joule heating, as we discuss later.

C. Kerr microscopy

Following the simulation results, a Kerr microscopy experiment was conducted to confirm the magnetic switch. Details of the Kerr microscopy experiment can be found in supplementary material S2, which presents experimental evidence of the effect of the bridge shape on creating stable domain formation near the tip apex. For this work, we studied more than 10 devices with small variations in the bridge width, but all on the micro-scale using FIB processing. We note that the shape of the bridge influences the domain stability as discussed in supplementary material S2. The gray and black shades in Figs. 2(d), 2(e), 2(g), and 2(h) show the Co domains that maintain their initial orientations before the pulse upon the application of a current pulse. Areas with false colors display the reaction of the Co domains to I_p. Figures 2(c) and 2(f) illustrate the orientation in the vertical direction using a blue-to-yellow color scale. Figures 2(d) and 2(g) depict the domain orientation in the horizontal direction, represented by a pink-to-green color scale. The domain is primarily confined to the bridge region, as only here is the current density high enough to cause Co domain reversal. Along the FIB bridge's length, the domains are inverted (pink and green), closely matching the numerical simulations in Figs. 2(c) and 2(f), supporting the realization of tip magnetization control, solely by a current pulse.

D. Numerical calculation of the thermal response and experimental validation of device stability

After applying I_p, the temperature increase should be minimal because it would hamper the operation in UHV and degrade the metallic layers of the tip. Examples and solution by metallic layer composition to prevent tip degradation are discussed in supplementary material S1. Hence, we modeled the (transient) temperature response of the tip for I_p =150 mA for an upper limit of the thermal increase. Figure 3(a) compares the simulated spatial current density across the bridge for a I_p of 160 ns, with the thermal profile. As expected, the current density is highest near the shortest width of the metallic film and is on the order of 10^{11} Am^{-2}. However, the maximum temperature increase is observed to be only 50 K, which means that operation in UHV is possible and would minimize Joule heating damage to the metallic films. We experimentally pulsed several tips for tens of times, and no degradation was observed. The transient heating response was also simulated, with the results given in Fig. 3(b). Here, a 160 ns asymmetric double sigmoidal pulse is simulated; see supplementary material S4 for pulse details. The temperature decreases rapidly within a microsecond as a result of efficient thermal dissipation of the Si substrate.

We examined how the substrate capping material, specifically a Si wafer with either a SiO_2 or MgO coating, influences thermal dissipation. These findings are further elaborated in supplementary material S1 and S4. It was discovered that MgO greatly improves thermal dissipation, thereby inhibiting thermal decomposition of the film from excessive joule heating, a problem noted in devices with SiO_2 layers. The stability of the tip was tested by applying many pules (>25 per device) of current amplitude larger than

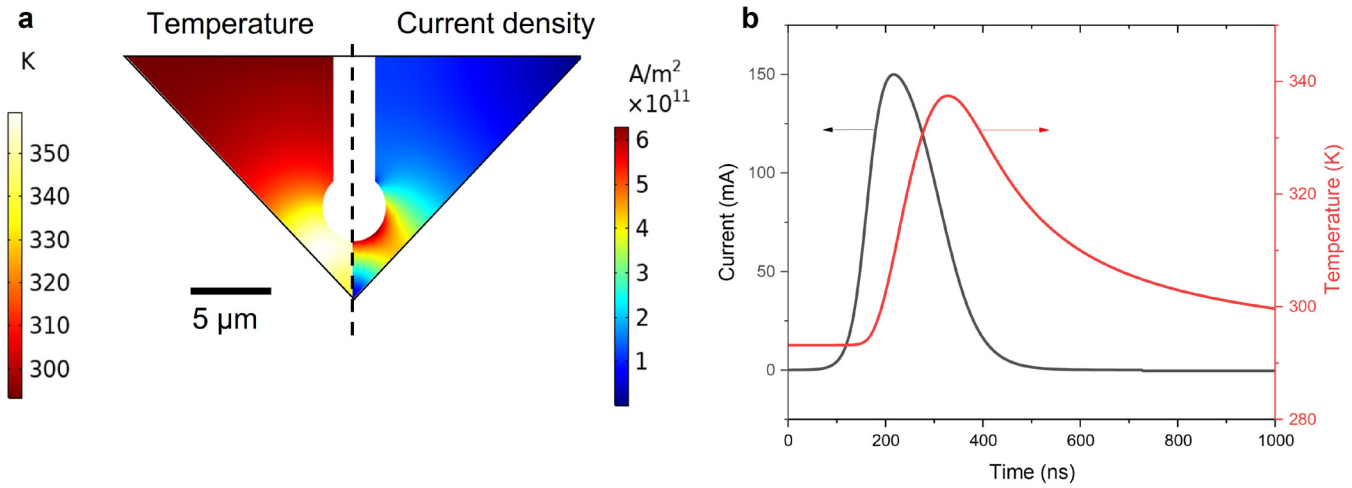

FIG. 3. Numerical study of the thermal response. (a) On the right, the calculated current density across the bridge for a current pulse of 150 mA. The current density increases up to 6×10^{11} Am^{-2} at the smallest section of the bridge. On the left, the corresponding temperature profile. (b) The current pulse I_p has to form an asymmetric double sigmoidal function plotted as the black curve. With a FWHM of 160 ns and a peak value of 150 mA. The transient temperature response, red curve, shows a rapid decay of the temperature, highlighting the efficient thermal dissipation of the bridge and ensuring mechanical stability.

150 mA. No notable degradation of tip bridge structure was noted. Furthermore, the enhanced stability could be leveraged to apply alternating current signals to the tip. The details are discussed in supplementary material S8. We employed a 1 Hz waveform where the duration of elevated current densities over the bridge considerably exceeded the nanoscale single pulses. As a result, these devices experienced significantly increased heat production over extended periods. Nonetheless, no notable degradation effects were observed. We conducted this experiment using SM-PP devices with bridge widths ranging from 4.5 to 6.7 μm. It was possible to observe the tip's magnetization responding to the AC current without any visible degradation. This method enables the alternating magnetization of the tip, offering potential advantages for a lock-in approach to monitor the MFM signal.

In summary of the initial segment of this study, the design and fabrication of the SM-PP leads to a force sensor with a high Q-factor, using planar probe tips. Alongside tip magnetization controlled by current, it facilitates the examination of magnetic surface textures of LMO.[13,14] In the subsequent part of our research, we utilize the SM-PP sensor to saturate and visualize the weak FM nanometer-scale islands present in an epitaxial ultrathin film of LMO on $SrTiO_3$ (STO).

E. MFM with the SM-PP sensor

We studied a 6 u.c. LMO on STO sample fabricated by the procedure of Ref. 13 and their characterization according to their supplementary material. The magnetic texture of a 6 u.c. LMO on STO sample was imaged with our MFM operating both below ($T = 100$ K) and above ($T = 30$ K) of LMO's $T_c = 115$ K.[13] The first aim was to identify the AF and weak-FM texture distribution across the surface. Second, we investigated whether the SM-PP was able to magnetize magnetic islands by the tip's oriented stray field exceeding 300 mT, see supplementary material S4, and this should lead to the observation of the magnetic islands with a lateral scale between 10 and 20 nm[14] or even smaller. The same SM-PP sensor was used for all imaging, with frequency modulation (FM) feedback. The scanning parameters are kept constant throughout all the measurements; see supplementary material S5 for methods and experimental details.

First, we scanned at a temperature of 100 K and imaged a plateau of the LMO/STO_3 stepped surface. The 90×90 nm topography images are given in Fig. 4(a) and demonstrates a LMO film RMS roughness S_q of 32 pm. Although the surface of LMO can show several u.c. surface height corrugations, which is a known surface feature for manganites.[30,31] The lateral resolution in topography is influenced by the relatively large amplitude of 10 nm used to detect the long-range magnetic force. Although other factors such as tip radius, the high Q-factor and the short tip-sample distance also influences the resolution. Ideally, a small amplitude would be used for high-resolution topography and a large amplitude for lifting-mode magnetic imaging.[26] We leave this for future work, as currently this approach of consecutively switching of the amplitude introduced a large drift in our setup.

After obtaining the local topography, we switched to MFM. The MFM signal was first acquired with a multi-domain, closed flux tip, where negligible out-of-plane oriented stray field should interact with the sample magnetic domains. Indeed, Fig. 4(b) shows that no MFM signal could be measured below the noise level of 1.5 mHz. The lack of topography cross talk in the lift mode image also demonstrates that the lateral variation of the electrostatic force is negligible.

Subsequently, the tip was pulsed by a 160 mA current pulse for 205 ns, which aligned the tip domain in the downward position, as indicated schematically in Fig. 4(c) and confirmed with Kerr microscopy prior. For safety, the tip was retracted by 0.5μm from

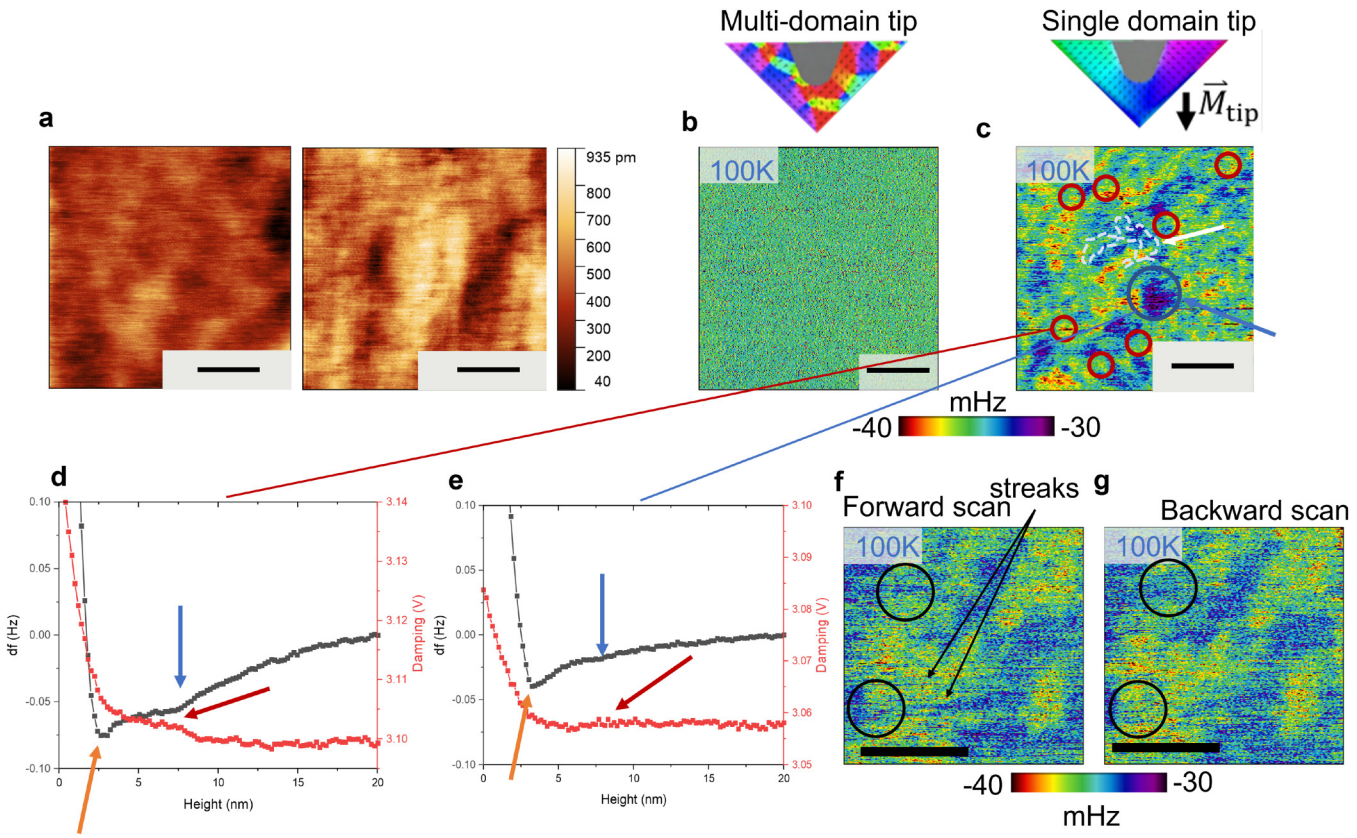

FIG. 4. MFM with the SM-PP sensor on 6 u.c. LMO/STO. (a) Topographic images of LMO. (b) Multi-domain tip state MFM measurement at 100 K showing no magnetic contrast.(c) The SM-PP tip is magnetized into a single domain. MFM imaging reveals spatially inhomogeneous magnetic contrast at 100 K. (d) Typical force-distance (F-z) spectroscopy and damping (voltage) signal taken at red areas of c. F-z spectroscopy shows a sudden kink in the attractive regime as highlighted with the blue arrow. The orange arrow indicated short range vdW forces. The damping signal (red line) is simultaneously taken, showing a sudden change in dissipation as indicated with the red arrow, (e) F-z spectroscopy and damping signal taken at a blue spot of c, showing significant reduction in sudden dissipation and force changes at the blue and red arrow, compared to d. (f) and (g) Magnetic features observed with a poled tip. The tip's stray field induces local magnetic domain perturbation (streaks) as indicated with the black circles and arrows. The forward and backward scan are compared. In all images, the black scale bar is equal to 30 nm.

the surface during the pulse, which can lead to a lateral drift of around 10 nm in our SPM at these temperatures. With the magnetically oriented tip, we continue MFM imaging at 100 K and observed a complex landscape of magnetic textures throughout the scanned area, as given in Fig. 4(c). The smallest magnetic objects are highlighted with red circles in Fig. 4(c), which also correspond to the strongest attractive magnetic forces. These features have on average a diameter of 10 nm. We attribute these area's as tip stray field induced magnetized domains. Observing the nominal size, it is very likely that these correspond to the weak FM textures,[14] even at 100 K. Performing force-distance (F-z) spectroscopy on the red islands of Fig. 4(d) showed complex behavior and provides more evidence for weak FM properties. The tip was retracted up to 20 nm above the surface and then lowered until a notable repulsive fore was observed. The frequency shift *df* was measured during spectroscopy. Evidence of the surface magnetization induced by the tip stray field is given in Fig. 4(d). We observe four distinct regimes; first, we note long-range attractive forces between 20 and 8 nm. This can be assigned to long range electrostatic forces, which do not change laterally. Around 7.5 nm, a sudden negative change in *df* is observed as indicated with a blue arrow in the figure. We attribute this to the significant increase of the magnetic field the sample experiences as the SM-PP tip approaches the weak FM domain and hence saturating it. At 3.4nm, indicated with an orange arrow, the attractive van der Waals force region is noted. At very small tip-sample distances, *df* becomes positive evidence of repulsive forces.

We also measured damping, a sign of energy loss via the local magnetization change of weak FM islands.[7] In Fig. 4(d), the red curve shows a sudden increase in damping, as indicated by the red arrow in the figure. Likely, at this distance the weak FM islands are magnetized periodically as the tip oscillates up and down, which requires constant input of energy supplied by the tip oscillation feedback system. For comparison, Fig. 4(e) shows the same F-z spectroscopy experiment performed on the blue areas of Fig. 4(c). Less perturbation of the attractive force *df* is observed, and no

measurable change in dissipation is observed, as highlighted with the colored arrows. We conjecture that those blue-colored areas are the antiferromagnetic domains.

Generally, the weak FM features (colored red) are embedded in magnetic labyrinth-like domains colored yellow/green in Fig. 4(c). These domains are continuous and spread across the surface. Furthermore, they have a smaller attractive force than the weak FM areas. The areas depicted in blue are observed in two distinct regimes. First, we note distributed areas highlighted with the dashed white line. Second, blue circular like textures are noted as highlighted with the blue circle. These textures show very little attractive frequency shift. Hence, excluding electrostatic forces, as these are constant across the surface, these domains form an antiferromagnetic texture, corroborating the SSM observations of Wang *et al.*[13] and Anahory *et al.*[14]

Furthermore, we note that the tip-stray field can induce local magnetic perturbations in the real-space imaging. By comparing the forward and the backward scan, Figs. 4(f) and 4(g), the areas highlighted in the black circle show a clear distinction between the two images. We conjecture that the field from the tip perturbed the local weak FM domains. This would also be in agreement with the observation of streaklines as indicated with the arrows.

We demonstrated a sharp contrast between the MFM imaging capabilities of the magnetic tip's multidomain and single-domain states. As expected from a weak and unknown oriented tip magnetic stray field, we initially could not detect an MFM signal above the noise floor at either 300 K or 100 K, as shown in supplementary material S6. Following the switch from tip magnetization to a single-domain state, we finally obtained an MFM map with a lateral resolution better than 10 nm, as seen from a line trace in supplementary material S7.

III. CONCLUSION AND OUTLOOK

In conclusion, the results offer strong indications of the imaging capabilities of the magnetically controllable SM-PP sensor for weak FM islands with a resolution higher than 10 nm. First, we achieved repeatable control over the magnetization at the SM-PP tip with a single domain state at the tip apex by integrating microscale current pathway. This tip-on-chip design is enabled by using planar probe like tips placed on a quartz tuning fork for integration in ultra-high vacuum. Following, we demonstrated imaging of a complex magnetic texture of epitaxial $LaMnO_3$ with nanometer scale identification of weak FM islands using the SM-PP sensor, confirming the existence of sub 10 nm weak FM islands embedded in a non-magnetic matrix near the Curie temperature. The tip-on-chip approach offers a viable pathway for future tip-integrated applications. Such, the SM-PP can be combined with scanning tunneling microscopy functionality because of the tip metallic layers and electrode accessibility of the tuning fork. In this way, we can combine ultra-high lateral resolution imaging of conductive metal-oxide perovskites and measure the long range MFM forces without the need to switch to different setups. This possibility opens up an approach to disentangle the atomic-scale structure and long-range magnetic ordering relations of transition-metal oxides for application in spintronic and catalytic devices. Considering its enhanced sensitivity, the widened scope of tip-on-chip design can convert the MFM/AFM from a surface analysis tool with passive probes to a more sophisticated device with active complex probes for characterization, e.g., on-chip nitrogen-vacancy centers diamond tips as quantum sensors for detecting ultra-small magnetic fields[32,33] or currents.[24]

SUPPLEMENTARY MATERIAL

See the supplementary material for the fabrication procedure of the planar probe with characterization of the film roughness, film engineering to prevent Joule heating, Kerr Microscopy experiment to image the single domain state near the tip apex after a current pulse of a SM-PP sensor, discussion of the QTF function of MFM, numerical calculations of the thermal and magnetic properties of the sensor, detailed experimental procedure for MFM imaging in UHV, MFM imaging below and above T_c and analysis of the obtainable lateral magnetic imaging resolution.

ACKNOWLEDGMENTS

The authors thank W. Dijkstra for assistance in both the modification of the UHV-SPM and fabrication of the custom pulse generator. Special thanks to H. Hilgenkamp of University of Twente, Netherlands, for providing the 6 u.c. $LaMnO_3$ thin film on the $SrTiO_3$ sample. This study was supported by NWO-TTW under Project No. 14715. O. Kurnosikov acknowledges support from ANR-15-IDEX-04-LUE CAP-MAT by the FEDER-FSE Lorraine et Massif Vosges 2014–2020. Financial support from the Eindhoven University of Technology is acknowledged.

AUTHOR DECLARATIONS

Conflict of Interest

The authors have no conflicts to disclose.

Author Contributions

Michael Verhage: Conceptualization (equal); Data curation (equal); Formal analysis (equal); Investigation (equal); Software (equal); Supervision (equal); Validation (equal); Visualization (equal); Writing – original draft (equal); Writing – review & editing (equal). **H. Tunç Çiftçi:** Conceptualization (equal); Data curation (equal); Formal analysis (equal); Investigation (equal); Supervision (equal); Validation (equal); Visualization (equal); Writing – original draft (supporting); Writing – review & editing (supporting). **Michiel Reul:** Data curation (supporting); Formal analysis (supporting); Software (equal); Visualization (supporting); Writing – original draft (supporting). **Tamar Cromwijk:** Data curation (supporting); Formal analysis (supporting); Investigation (equal); Software (equal); Writing – original draft (supporting). **Thijs J. N. van Stralen:** Data curation (supporting); Formal analysis (supporting); Investigation (supporting); Software (equal); Writing – original draft (supporting). **Bert Koopmans:** Conceptualization (equal); Funding acquisition (lead); Methodology (supporting); Project administration (lead); Resources (lead); Software (supporting); Supervision (lead); Validation (supporting); Writing – original draft (supporting); Writing – review & editing (supporting). **Oleg Kurnosikov:** Conceptualization (equal);

Formal analysis (equal); Funding acquisition (equal); Investigation (equal); Methodology (equal); Supervision (equal); Validation (supporting); Writing – original draft (supporting); Writing – review & editing (supporting). **Kees Flipse:** Conceptualization (equal); Data curation (equal); Formal analysis (equal); Funding acquisition (equal); Investigation (equal); Supervision (equal); Validation (equal); Writing – original draft (equal); Writing – review & editing (equal).

DATA AVAILABILITY

The data that support the findings of this study are available from the corresponding author upon reasonable request.

REFERENCES

[1]O. Kazakova, R. Puttock, C. Barton, H. Corte-León, M. Jaafar, V. Neu, and A. Asenjo, "Frontiers of magnetic force microscopy," J. Appl. Phys. **125**, 060901 (2019).

[2]H. J. Hug, B. Stiefel, P. J. A. Van Schendel, A. Moser, R. Hofer, S. Martin, H.-J. Güntherodt, S. Porthun, L. Abelmann, J. C. Lodder, G. Bochi, and R. C. O'Handley, "Quantitative magnetic force microscopy on perpendicularly magnetized samples," J. Appl. Phys. **83**, 5609–5620 (1998).

[3]A. Casiraghi, H. Corte-León, M. Vafaee, F. Garcia-Sanchez, G. Durin, M. Pasquale, G. Jakob, M. Kläui, and O. Kazakova, "Individual skyrmion manipulation by local magnetic field gradients," Commun. Phys. **2**, 145 (2019).

[4]E. Albisetti, D. Petti, M. Pancaldi, M. Madami, S. Tacchi, J. Curtis, W. P. King, A. Papp, G. Csaba, W. Porod, P. Vavassori, E. Riedo, and R. Bertacco, "Nanopatterning reconfigurable magnetic landscapes via thermally assisted scanning probe lithography," Nat. Nanotechnol. **11**, 545–551 (2016).

[5]J. C. Gartside, D. M. Arroo, D. M. Burn, V. L. Bemmer, A. Moskalenko, L. F. Cohen, and W. R. Branford, "Realization of ground state in artificial kagome spin ice via topological defect-driven magnetic writing," Nat. Nanotechnol. **13**, 53–58 (2018).

[6]S. Schreiber, M. Savla, D. Pelekhov, D. Iscru, C. Selcu, P. Hammel, and G. Agarwal, "Magnetic force microscopy of superparamagnetic nanoparticles," Small **4**, 270–278 (2008).

[7]B. Torre, G. Bertoni, D. Fragouli, A. Falqui, M. Salerno, A. Diaspro, R. Cingolani, and A. Athanassiou, "Magnetic force microscopy and energy loss imaging of superparamagnetic iron oxide nanoparticles," Sci. Rep. **1**, 202 (2011).

[8]L. Angeloni, D. Passeri, M. Reggente, D. Mantovani, and M. Rossi, "Removal of electrostatic artifacts in magnetic force microscopy by controlled magnetization of the tip: Application to superparamagnetic nanoparticles," Sci. Rep. **6**, 26293 (2016).

[9]A. Krivcov, T. Junkers, and H. Möbius, "Understanding electrostatic and magnetic forces in magnetic force microscopy: Towards single superparamagnetic nanoparticle resolution," J. Phys. Commun. **2**, 075019 (2018).

[10]V. Cambel, D. Gregušová, P. Eliáš, J. Fedor, I. Kostič, J. Maňka, and P. Ballo, "Switching magnetization magnetic force microscopy—An alternative to conventional lift-mode MFM," J. Electr. Eng. **62**, 37–43 (2011).

[11]V. Cambel, M. Precner, J. Fedor, J. Šoltýs, J. Tóbik, T. Ščepka, and G. Karapetrov, "High resolution switching magnetization magnetic force microscopy," Appl. Phys. Lett. **102**, 062405 (2013).

[12]T. Wren, R. Puttock, B. Gribkov, S. Vdovichev, and O. Kazakova, "Switchable bi-stable multilayer magnetic probes for imaging of soft magnetic structures," Ultramicroscopy **179**, 41–46 (2017).

[13]X. R. Wang, C. J. Li, W. M. Lü, T. R. Paudel, D. P. Leusink, M. Hoek, N. Poccia, A. Vailionis, T. Venkatesan, J. M. D. Coey, E. Y. Tsymbal, A. Ariando, and H. Hilgenkamp, "Imaging and control of ferromagnetism in $LaMnO_3$/$SrTiO_3$ heterostructures," Science **349**, 716–719 (2015).

[14]Y. Anahory, L. Embon, C. J. Li, S. Banerjee, A. Meltzer, H. R. Naren, A. Yakovenko, J. Cuppens, Y. Myasoedov, M. L. Rappaport, M. E. Huber, K. Michaeli, T. Venkatesan, A. Ariando, and E. Zeldov, "Emergent nanoscale superparamagnetism at oxide interfaces," Nat. Commun. **7**, 12566 (2016).

[15]H. Corte-León, L. A. Rodríguez, M. Pancaldi, C. Gatel, D. Cox, E. Snoeck, V. Antonov, P. Vavassori, and O. Kazakova, "Magnetic imaging using geometrically constrained nano-domain walls," Nanoscale **11**, 4478–4488 (2019).

[16]B. Sakar, Y. Liu, S. Sievers, V. Neu, J. Lang, C. Osterkamp, M. L. Markham, O. Öztürk, F. Jelezko, and H. W. Schumacher, "Quantum calibrated magnetic force microscopy," Phys. Rev. B **104**, 214427 (2021).

[17]H. Corte-León, V. Neu, A. Manzin, C. Barton, Y. Tang, M. Gerken, P. Klapetek, H. W. Schumacher, and O. Kazakova, "Comparison and validation of different magnetic force microscopy calibration schemes," Small **16**, 1906144 (2020).

[18]V. Panchal, H. Corte-León, B. Gribkov, L. A. Rodriguez, E. Snoeck, A. Manzin, E. Simonetto, S. Vock, V. Neu, and O. Kazakova, "Calibration of multi-layered probes with low/high magnetic moments," Sci. Rep. **7**, 7224 (2017).

[19]T. Siahaan, O. Kurnosikov, B. Barcones, H. J. M. Swagten, and B. Koopmans, "Cleaved thin-film probes for scanning tunneling microscopy," Nanotechnology **27**, 03LT01 (2016).

[20]H. T. Ciftci, L. P. Van, B. Koopmans, and O. Kurnosikov, "Polymer patterning with self-heating atomic force microscope probes," J. Phys. Chem. A **123**, 8036–8042 (2019).

[21]M. Leeuwenhoek, F. Groenewoud, K. Van Oosten, T. Benschop, M. P. Allan, and S. Gröblacher, "Fabrication of on-chip probes for double-tip scanning tunneling microscopy," Microsyst. Nanoeng. **6**, 99 (2020).

[22]A. Finkler, D. Vasyukov, Y. Segev, L. Neeman, Y. Anahory, Y. Myasoedov, M. L. Rappaport, M. E. Huber, J. Martin, A. Yacoby, and E. Zeldov, "Nano-sized SQUID-on-tip for scanning probe microscopy," J. Phys.: Conf. Ser. **400**, 052004 (2012).

[23]Y. Zhang, W. Zhu, F. Hui, M. Lanza, T. Borca-Tasciuc, and M. Munoz Rojo, "A review on principles and applications of scanning thermal microscopy (SThM)," Adv. Funct. Mater. **30**, 1900892 (2020).

[24]A. Ariyaratne, D. Bluvstein, B. A. Myers, and A. C. B. Jayich, "Nanoscale electrical conductivity imaging using a nitrogen-vacancy center in diamond," Nat. Commun. **9**, 2406 (2018).

[25]H. T. Çiftçi, M. Verhage, T. Cromwijk, L. Pham Van, B. Koopmans, K. Flipse, and O. Kurnosikov, "Enhancing sensitivity in atomic force microscopy for planar tip-on-chip probes," Microsyst. Nanoeng. **8**, 51 (2022).

[26]M. Schneiderbauer, D. Wastl, and F. J. Giessibl, "qPlus magnetic force microscopy in frequency-modulation mode with millihertz resolution, Beilstein J. Nanotechnol. **3**, 174–178 (2012).

[27]H. T. Ciftci, "Functionalized planar probe for advanced scanning probe microscopy," Ph.D. thesis (Eindhoven University of Technology, Eindhoven, 2022).

[28]H. Ooe, T. Sakuishi, M. Nogami, M. Tomitori, and T. Arai, "Resonance frequency-retuned quartz tuning fork as a force sensor for noncontact atomic force microscopy," Appl. Phys. Lett. **105**, 043107 (2014).

[29]F. J. Giessibl, "The qPlus sensor, a powerful core for the atomic force microscope," Rev. Sci. Instrum. **90**, 011101 (2019).

[30]A. Gambardella, P. Graziosi, I. Bergenti, M. Prezioso, D. Pullini, S. Milita, F. Biscarini, and V. A. Dediu, "Surface nanostructures in manganite films," Sci. Rep. **4**, 5353 (2014).

[31]M. Verhage, E. Van Der Minne, E. M. Kiens, L. Korol, R. J. Spiteri, G. Koster, R. J. Green, C. Baeumer, and C. F. J. Flipse, "Electronic and structural disorder of the epitaxial $La_{0.67}Sr_{0.33}MnO_3$ surface," ACS Appl. Mater. Interfaces **16**, 21273–21282 (2024).

[32]F. Casola, T. Van Der Sar, and A. Yacoby, "Probing condensed matter physics with magnetometry based on nitrogen-vacancy centres in diamond," Nat. Rev. Mater. **3**, 17088 (2018).

[33]A. J. Healey, S. C. Scholten, T. Yang, J. A. Scott, G. J. Abrahams, I. O. Robertson, X. F. Hou, Y. F. Guo, S. Rahman, Y. Lu, M. Kianinia, I. Aharonovich, and J.-P. Tetienne, "Quantum microscopy with van der Waals heterostructures," Nat. Phys. **19**, 87–91 (2023).